Chemical Science

ROYAL SOCIETY OF CHEMISTRY

EDGE ARTICLE

View Article Online
View Journal

Cite this: DOI: 10.1039/d6sc00740f

All publication charges for this article have been paid for by the Royal Society of Chemistry

Anion-sublattice engineering of Li_3PS_4:Br and I incorporation enhances ionic conductivity and Li-metal compatibility

Tej P. Poudel,†[abc] Michael J. Deck,†[bc] Ifeoluwa P. Oyekunle,[bc] Pawan K. Ojha,[bc] Bright O. Ogbolu,[bc] Islamiyat Ojelade,[bc] Thilina N. D. D. Gamaralagale,[bc] Erica Truong,[bc] Yongkang Jin,[bc] Amirhossein Zareihassangheshlaghi[b] and Yan-Yan Hu *[abc]

Received 27th January 2026
Accepted 14th April 2026

DOI: 10.1039/d6sc00740f

rsc.li/chemical-science

All-solid-state batteries (ASSBs) are promising to enhance the safety and energy density of rechargeable batteries. Li_3PS_4 remains one of the most viable solid electrolytes (SEs) for all-solid-state lithium batteries. However, its low ionic conductivity and poor stability limit its commercial use. In this work, we introduce lithium bromide (LiBr) and lithium iodide (LiI) into the anionic sublattice of Li_3PS_4 to induce local disorder. An eightfold increase in ionic conductivity to 4.36 mS cm^{-1} at 25 °C is achieved with the $2Li_3PS_4$:LiBr:LiI composition. $2Li_3PS_4$:LiBr:LiI also exhibits a high room temperature critical current density of 0.92 mA cm^{-2} and improved electrochemical stability against lithium metal. The half-cell fabricated with $2Li_3PS_4$:LiBr:LiI as the separator and TiS_2 as the active cathode material shows significantly better rate and long-term cycling performance compared to cells based on Li_3PS_4. Solid-state NMR and Raman spectroscopy indicate the formation of bridging PS_4^{3-} tetrahedra facilitated by the incorporation of I^- and Br^-. This study further highlights the advantages of strategic halide incorporation in thiophosphate electrolytes to enhance the performance of Li_3PS_4-based SEs and, in turn, ASSBs.

Introduction

All-solid-state batteries (ASSBs) are a promising way to improve the energy density and safety of rechargeable batteries. Solid electrolyte(s) (SEs) are a critical component in ASSBs. Li_3PS_4 remains one of the most promising solid electrolytes for all-solid-state lithium batteries, primarily due to its cost-effectiveness, mechanical processability, and compatibility with lithium metal. However, its practical application faces key challenges: relatively low ionic conductivity (<0.5 mS cm^{-1}) and stability issues. Ongoing research with doping, glass–ceramic approaches, and interface engineering has made progress in addressing these challenges.[1–5] With continued improvements, Li_3PS_4 (or modified variants) could form the backbone of next-generation solid-state batteries – offering high energy density, safety, and potentially long cycle life.

Our previous work has demonstrated that incorporating mixed anions, such as O and Br, into the LPS structural framework significantly enhances Li^+ ionic conductivity, stability, and critical current density.[1,2] The improvement in Li^+ transport in the mixed-anion SEs is attributed to increased nanoscale local disorder, which creates a flattened energy landscape.[6–8] Further introduction of local disorder, *i.e.*, the incorporation of mixed anions such as halide combinations, can yield higher-performing SEs, as is the case for $Li_{5.3}PS_{4.3}Cl_{0.3}Br_{0.7}$.[9]

Herein, we synthesize and investigate the Li^+ dynamics, electrochemical performance, and local structures of xLi_3PS_4:yLiBr:zLiI. Electrochemical impedance spectroscopy (EIS) determined a maximum ionic conductivity of 4.36 mS cm^{-1} at 25 °C and a minimum activation energy of 0.29 eV for sintered $2Li_3PS_4$:LiBr:LiI. Symmetrical galvanostatic cycling revealed significantly improved electrochemical stability against Li metal with a high critical current density (CCD). Compared to sintered $2Li_3PS_4$:LiBr:LiI (LPSBI-sin), as-milled LPSBI (LPSBI-as) has a lower ionic conductivity of 1.4 mS cm^{-1} and lower CCD; however, it has a better electrochemical stability against Li metal. When assembled into a stacked pellet using the Li|LPSBI-as|LPSBI-sin|LPSBI-as|Li setup, the CCD is further improved. Cyclic voltammograms indicate that the effective electrochemical stability window is retained upon incorporation of halide salts into LPS. In ASSB half-cells using TiS_2 as cathode active material (CAM), the LPSBI-containing cell showed significantly improved rate performance and long-term cycling

[a]*Materials Science and Engineering Program, Florida State University, Tallahassee, FL 32310, USA. E-mail: yhu@fsu.edu*

[b]*Department of Chemistry and Biochemistry, Florida State University, Tallahassee, FL 32306, USA*

[c]*Center for Interdisciplinary Magnetic Resonance, National High Magnetic Field Laboratory, Tallahassee, FL 32310, USA*

† These authors contributed equally.

when compared to that using LPS. Powder X-ray diffraction (PXRD) indicates the absence of long-range order, and solid-state nuclear magnetic resonance spectroscopy (NMR) and Raman spectroscopy were used to elucidate the local environments of Li and P. This work highlights the use of mixed-halide lithium thiophosphate SEs to increase local disorder and enhance SE functional properties, thus facilitating the commercialization of ASSBs.

Materials and methods

Material synthesis

Li_2S, P_2S_5, LiBr, and LiI, were purchased from Sigma-Aldrich and stored in an argon-filled glovebox (Vacuum Technology). $x$$Li_3PS_4$:$y$LiBr:$z$LiI was synthesized through a high-energy ball milling technique followed by low-temperature heat treatment. First, the precursors were hand-ground to ensure a homogeneous mixture, followed by high-energy ball milling in a SPEX8000M for 20 h. The samples after ball milling were named "as-milled". The samples were then either pelletized in a 6 mm mold into ~1 mm thick pellets under ~300 MPa pressure or directly transferred into an evacuated quartz tube. Sintering was carried out at 200 °C for 12 h at a ramping rate of 1 °C min^{-1}. The sintered pellet samples are named "sintered" hereafter. All synthesis processes were performed in an argon-filled glovebox (MBRAUN).

Material characterization

Impedance measurements. The pellet (either cold-pressed or sintered) was sandwiched between indium foils and assembled into an in-house-built cylindrical cell. EIS measurements were performed using a Gamry reference 600+ over a frequency range of 0.1 Hz to 5 MHz. Variable-temperature EIS (VT-EIS) measurements were also conducted over the temperature range of −20 to 120 °C.

DC polarization. The same setup used for impedance measurements was used to perform DC polarization. The cell was allowed to equilibrate for 2.4 hours at 0.1 V. The current at the plateau was utilized to determine the electronic conductivity.

The DC polarization technique was also utilized to measure the effective ionic and electronic conductivity of the catholytes prepared for the TiS_2 half-cell cycling, according to the literature.[10] Effective electronic conductivity was measured using a SS|2SE:TiS_2|SS cell setup. 100 mg of the catholyte was pressed under 250 MPa for 10 s. The effective ionic conductivity of catholytes was measured utilizing a Li–In|LPSCl|2SE:TiS_2-|LPSCl|Li–In cell setup. 100 mg of catholyte was first pressed in the split cell at 250 MPa for 10 s, followed by pressing 60 mg of Li_6PS_5Cl on each side of the catholyte pellet at 250 MPa for another 10 s. Li–In alloy was used as the Li source, while Li_6PS_5Cl layers were used as the electron-blocking electrodes. The calculated resistance from the current plateau is used to calculate the effective conductivity, σ_{eff}, according to $\sigma_{eff} = \frac{l}{R \times A}$ where l is the thickness of the catholyte pellet, R is the resistance, and A is the area of the electrodes.

Critical current density measurement and symmetric-cell cycling. In-house-built PEEK split cells were used to measure critical current density (CCD) and perform long-term symmetric cycling. CCD measurements were performed in two different cell setups. For the first CCD setup, the Li|SE|Li symmetric cells were prepared by pressing ~120 mg of SE between $\frac{1}{4}$-in-diameter Li foils of ~0.1 mm thickness. Similar cells were utilized to perform extended symmetric cycling. For the second CCD setup, three layers of SEs – Li|SE-as|SE-sin|SE-as|Li were utilized. A layer of 75 mg of SE-sin was pressed under 100 MPa, followed by pressing 25 mg of SE-as on both sides of SE-sin at 300 MPa for 10 s. All the CCD and extended symmetric cells were cycled under a stack pressure of 5 MPa at room temperature (~22 °C).

ASSB assembly. 100 mg of SE was pressed in a 10 mm in-house-built split cell at 250 MPa for 10 s to function as the ASSB separator layer. For CV and galvanostatic employing carbon-composite half-cells, 12 mg of the manually mixed 3SE:carbon (Super P (SP)) was evenly spread onto one surface of the pellet and pressed at 300 MPa for 10 s. Li–In alloy was used as the anode on the opposite side of the pellet. CV measurements were performed at a scan rate of 0.2 mV s^{-1} over a voltage range of 0–4 V *vs.* Li–In. A current density of 0.064 mA cm^{-2} was applied for galvanostatic cycling in the same voltage range as in CV measurements. For 2SE:TiS_2 half-cells, 12 mg of hand-mixed catholyte (2SE:TiS_2) was carefully spread onto a side of the pellet and pressed at 250 MPa for 10 s, corresponding to an approximate areal capacity of 1.25 mAh cm^{-2}. Li–In alloy was used as the anode on the other side of the pellet. After sealing with vacuum grease, cells were cycled under ~30 MPa stack pressure at 22 °C between 1–2.5 V *vs.* Li–In. For more details, please see our previous reports.[1,2,11–14]

Scanning electron microscopy. Scanning electron microscope (SEM) images were obtained using a JEOL JSM-IT800 electron microscope (FE-SEM). Approximately 20 mg of sample powder was pressed in a 6 mm diameter stainless-steel mold at 300 MPa inside an argon-filled glovebox. The obtained pellet was then placed on carbon tape in a vacuum-sealed sample holder. The sample holder was transferred into the exchange chamber of the JEOL JSM-IT800 and evacuated to prevent air contamination of the pellets. An accelerating voltage of 5 kV was used, and SEM images were taken at a magnification of 5000× for 1 minute each.

Powder X-ray diffraction. For powder X-ray diffraction analysis, samples were prepared on a zero-background sample holder covered with a Kapton film and vacuum grease to protect them from the ambient environment. The diffractograms were collected on a Rigaku Smartlab using Cu-Kα radiation over 10–80° with a step size of 0.03° at a scan rate of 2.5 min^{-1}.

Solid-state nuclear magnetic resonance spectroscopy. ^{6,7}Li solid-state NMR experiments were performed on a Bruker 11.74 T NMR spectrometer at a spin rate of 24 kHz. Single-pulse ^{6,7}Li and spin-echo ^{31}P magic-angle-spinning (MAS) NMR experiments were conducted on the samples, with a 90° pulse of 3.95 μs and a recycle delay of 50 s. ^{7}Li spin-lattice relaxation, T_1, was

conducted using the inversion recovery method. The ^{6,7}Li and ^{31}P shifts were referenced to LiCl(s) at −1.1 ppm and solid diammonium phosphate at 1.34 ppm, respectively. ^{7}Li and ^{31}P variable-temperature NMR experiments were performed on a 7.05 T Bruker NMR spectrometer at a spin rate of 10 kHz. *In situ* variable-temperature ^{7}Li and ^{31}P MAS NMR measurements were conducted over the temperature range of 298–343 K using a Bruker Avance III 300 spectrometer, at Larmor frequencies of 116.6 MHz for ^{7}Li and 121.5 MHz for ^{31}P, respectively.

Raman spectroscopy measurements. Raman spectra were collected using a Horiba JY LabRam HR Evolution Raman spectrograph with a 785 nm excitation laser and a grating size of 1800 g mm^{-1}.

Results and discussion

Superionic conductivity in mixed-halide lithium thiophosphates

Table S1 shows the various compositions of xLi$_3$PS$_4$:yLiBr:zLiI and the corresponding conductivities measured at 22 °C. The highest conductivity (1.41 mS cm^{-1}) was achieved for 2Li$_3$PS$_4$:LiBr:LiI (LPSBI-as) upon one-step ball milling synthesis, which was chosen as a model milled sample and denoted LPSBI-as. We sintered the milled SEs at 200 °C. Upon pellet sintering, a threefold increase in conductivity (4.36 mS cm^{-1}) was achieved for the best conductive milled composition (2Li$_3$PS$_4$:LiBr:LiI), denoted as LPSBI-sin.

Fig. 1a shows the Nyquist plots and equivalent circuit model fit of the fabricated SEs at 25 °C. From the resistances obtained from the fittings, 20-h high-energy milled Li$_3$PS$_4$ (LPS-as), LPSBI-as, and LPSBI-sin have room-temperature ionic conductivities of 0.58, 1.41, and 4.36 mS cm^{-1}, respectively. Variable temperature EIS was performed, and Arrhenius-type plots were obtained (Fig. 1b and S1). The Li$^+$ migration barrier (E_a), as determined from variable-temperature EIS measurements and an Arrhenius-type equation[15] (Fig. 1b), is 0.39 eV for LPS-as, 0.34 eV for LPSBI-as, and 0.29 eV for LPSBI-sin, with the data listed in Table 1. The enhanced ionic conductivity upon halide introduction is due to increased local disorder at the nanoscale, which lowers the energy barrier for Li$^+$ conduction.[16] The Nyquist plot at −20 °C, with an exemplary plot presented in Fig. 1c, shows only 1 semicircle at high frequency and indicates that the bulk and grain boundary conduction cannot be separated for all samples except for 4Li$_3$PS$_4$:3LiBr:LiI and 8Li$_3$PS$_4$:3LiBr:LiI. The high-frequency impedance response is assigned to the bulk, with a capacitance of ∼79 pF.[17,18] The medium-frequency semicircle is assigned to the grain boundary (GB) impedance response due to a capacitance of 0.3 nF for 4Li$_3$PS$_4$:3LiBr:LiI and 27 nF for 8Li$_3$PS$_4$:3LiBr:LiI. A low-frequency semicircle is assigned to the blocking electrode contribution, as is often the case for halide-containing SEs.[19] Fig. 1d shows the conductivity values for other as-milled and sintered compositions, confirming the maximum ionic conductivity and minimum E_a achieved in 2LPS:LiBr:LiI. Furthermore, sintered 2LPS:LiBr:LiI has the lowest Arrhenius prefactor among the compositions, indicating that E_a correlates strongly with conductivity (Fig. S1). Fig. S1 also shows the Nyquist plots of the less-conductive samples, their fits, and Arrhenius-type plots. The direct current (DC) polarization method with blocking electrodes was used to determine the electronic conductivity, as shown in Fig. S2. LPSBI-sin has an electronic conductivity of 1.82 × 10^{-9} S cm^{-1}.

Electrochemical performance of mixed-halide lithium thiophosphates

Critical current density (CCD) and symmetric-cell cycling. To determine the CCD and electrochemical stability against Li metal of the highest conducting as-milled and sintered SE compositions, symmetric galvanostatic cycling was performed, as shown in Fig. 2a–c. At 22 °C, the CCD is 0.34 mA cm^{-2} for Li|LPS-as|Li, 0.48 mA cm^{-2} for Li|LPSBI-as|Li, and 0.70 mA cm^{-2} for Li|LPSBI-sin|Li. The trend in CCD indicates better resistance to dendrite formation for LPSBI-as at high current densities.[20] To further assess the electrochemical stability against Li metal, long-term galvanostatic cycling was performed, as seen in Fig. 2d. The LPS-as cell shorts within 45 days of cycling at a current density of 0.1 mA cm^{-2}, whereas the LPSBI-as and LPSBI-sin cells do not fail for over 100 days, indicating improved electrochemical stability against Li metal, likely due to the stable LiX (X = Br, I) interface. The LPSBI-sin cell shows a slightly larger initial voltage upon cycling compared to the LPSBI-as cell; this is caused by the crushing of the LPSBI-sin pellet after heat treatment to assemble it into the in-house-built split cell for measurements. The crushing followed by cold-pressing results in the formation of grain boundaries and voids. The re-pelletized LPSBI-sin was evaluated with EIS measurements, with the equivalent circuit fitting shown in Fig. S3. The high-frequency semicircle has a capacitance on the order of 10^{-10} F, suggesting it is difficult to resolve the GB and bulk conductivities (2.01 mS cm^{-1}) upon cold pressing of LPSBI-sin. Furthermore, the LPSBI-sin cell shows a larger increase in voltage upon cycling, indicating it is less electrochemically stable against Li metal than LPSBI-as. With this in mind, we fabricated a cell using the following setup: Li|LPSBI-as|LPSBI-sin|LPSBI-as|Li and achieved a further improved CCD of 0.92 mA cm^{-2} (Fig. 2e). This demonstrates the strategic advantage of leveraging materials with the same elemental composition but with different processing to engineer improved SE performance.

Cyclic voltammetry and galvanostatic cycling. To assess the effective electrochemical stability window of LPSBI, cyclic voltammetry (CV) was first performed (Fig. S4) using the following setup: Li–In|SE|3SE:C. Carbon (Super P) was used in the cathode composite to improve electrical contact between the SE and the planar electrodes and to measure the onset oxidation voltage more accurately.[1,2,21] All 3 compositions, LPS, LPSBI-as, and LPSBI-sin, show a decrease in current after 1st cycle, as seen in Fig. S4a–c.

Comparing the 1st cycle of each composition (Fig. S4d) and starting with the cathodic sweep, a cathodic peak at around 1.8 V is attributed to S reduction. LPS-as exhibits the largest current for this peak. The cathodic peak at 1.8 V is smaller for LPSBI samples because they contain less sulfur. At lower voltages, the SE redox product, P, is lithiated to form Li$_3$P. For the

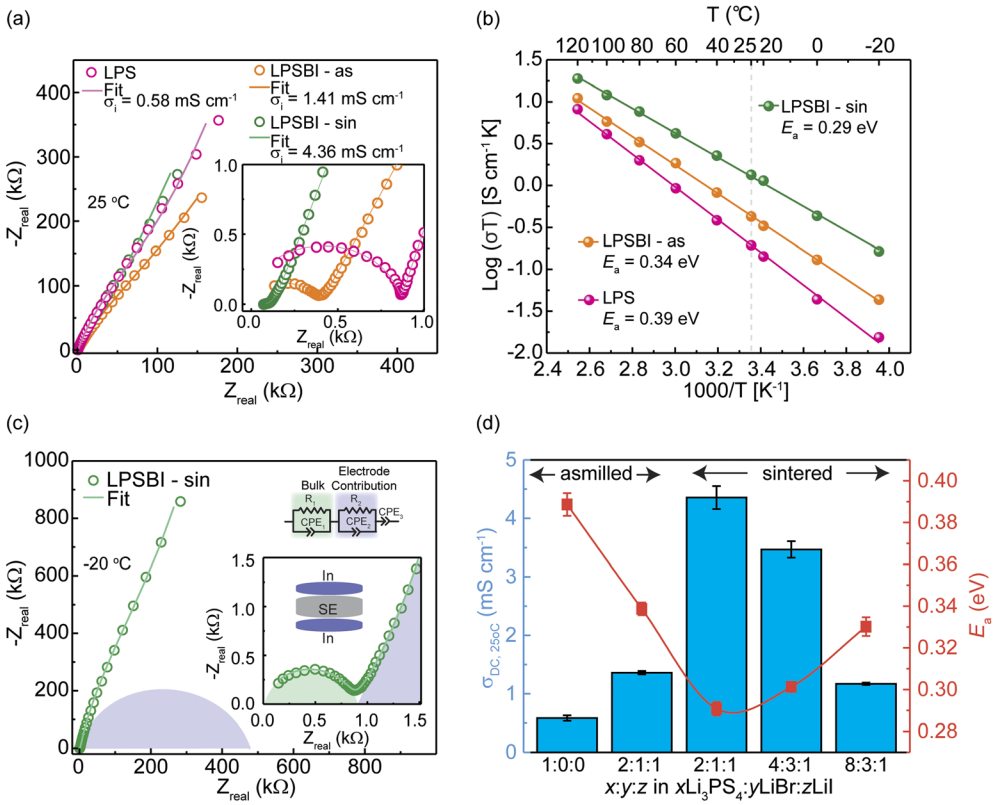

Fig. 1 EIS analysis of xLi$_3$PS$_4$:yLiBr:zLiI. (a) Nyquist plots (open circles), the corresponding fit (solid lines), and the resulting ionic conductivities of LPS, LPSBI-as, and LPSBI-sin. (b) Arrhenius-type plots of the respective SEs and activation energy; the gray dashed line is a visual guide for conductivities at 25 °C. (c) The representative equivalent circuit model for LPSBI-sin for the Nyquist plot at −20 °C. Two semicircles in the impedance response are observed, and the Nyquist plot is fitted with the $R/Q + R/Q + Q$ type equivalent circuit. The high-frequency semicircle corresponds to impedance from the bulk of the SE. The low-frequency semicircle is associated with impedance from the blocking electrode contribution, with a capacitance of 0.25 μF. (d) Ionic conductivity and activation energy of xLi$_3$PS$_4$:yLiBr:zLiI prepared using different strategies.

anodic sweep, the peak starting at ∼1.8 V *vs.* Li–In is assigned $S_x^{2-} \rightarrow S_x$.[11] The onset oxidation voltage, *i.e.*, the oxidation of PS_4^{3-}, begins at the voltage of ∼2.4 V *vs.* Li–In for all compositions and is consistent with previous reports for Li_3PS_4.[1,2,11]

To determine the reversible redox reactions of the SEs that contribute to overall capacity, identical cells as those from CV were assembled and galvanostatically cycled (Fig. S5). Over 85 cycles, the LPSBI-sin cell shows a higher charge/discharge capacity compared to the other cells. The LPSBI-sin cell shows an improved 1st discharge capacity of ∼175 mAh g_{SE}^{-1} compared to 145 mAh g_{SE}^{-1} for the LPS-as cell and 112 mAh g_{SE}^{-1} for the LPSBI-as cell. The irreversible capacity plateaus for the 1st cycle are the formation of a passivation layer, as extensively reported in the literature, and likely contribute to our TiS_2-containing cells' (see below) capacity being slightly greater than the theoretical value for Cycles 1 and 2.[1,2,11] From dQ/dV analysis (Fig. S6), it is evident that a greater amount of I^- oxidation is observed for LPSBI-as, which starts at ∼2.25 V *vs.* Li–In; this correlates well with the 1st charge capacity of the LPSBI-as cell being significantly larger than the 1st discharge, as well as when compared to the other SEs. The oxidation voltage of I^- was determined by using LiI as the active cathode, shown in Fig. S7. Notably, there is no indication of Br^- oxidation at >3 V *vs.* Li–In, consistent with our previous studies on halide-containing SEs.[1,12] On discharge, the plateau at 1.8 V is assigned to lithiation of elemental sulfur impurities from our synthesis process, as we typically observe and have reported for other Li_3PS_4-based solid electrolytes (as is also seen in our CV

Table 1 EIS analysis results of xLi$_3$PS$_4$:yLiBr:zLiI samples, including ionic conductivity at 25 °C, activation energy, and Arrhenius-type prefactor

Composition	$\sigma_{DC,25°C}$ [mS cm^{-1}]	$E_{a,DC}$ [eV]	Log(σ_0) [S cm^{-1} K^{-1}]
Li_3PS_4-as-milled	0.58 ± 0.05	0.388 ± 0.005	5.85 ± 0.09
2Li_3PS_4:LiBr:LiI – as-milled	1.41 ± 0.03	0.339 ± 0.003	5.36 ± 0.05
2Li_3PS_4:LiBr:LiI – sintered	4.36 ± 0.20	0.291 ± 0.003	5.02 ± 0.05
4Li_3PS_4:3LiBr:LiI – sintered	3.47 ± 0.14	0.301 ± 0.002	5.11 ± 0.04
8Li_3PS_4:3LiBr:1LiI – sintered	1.17 ± 0.02	0.330 ± 0.004	5.11 ± 0.07

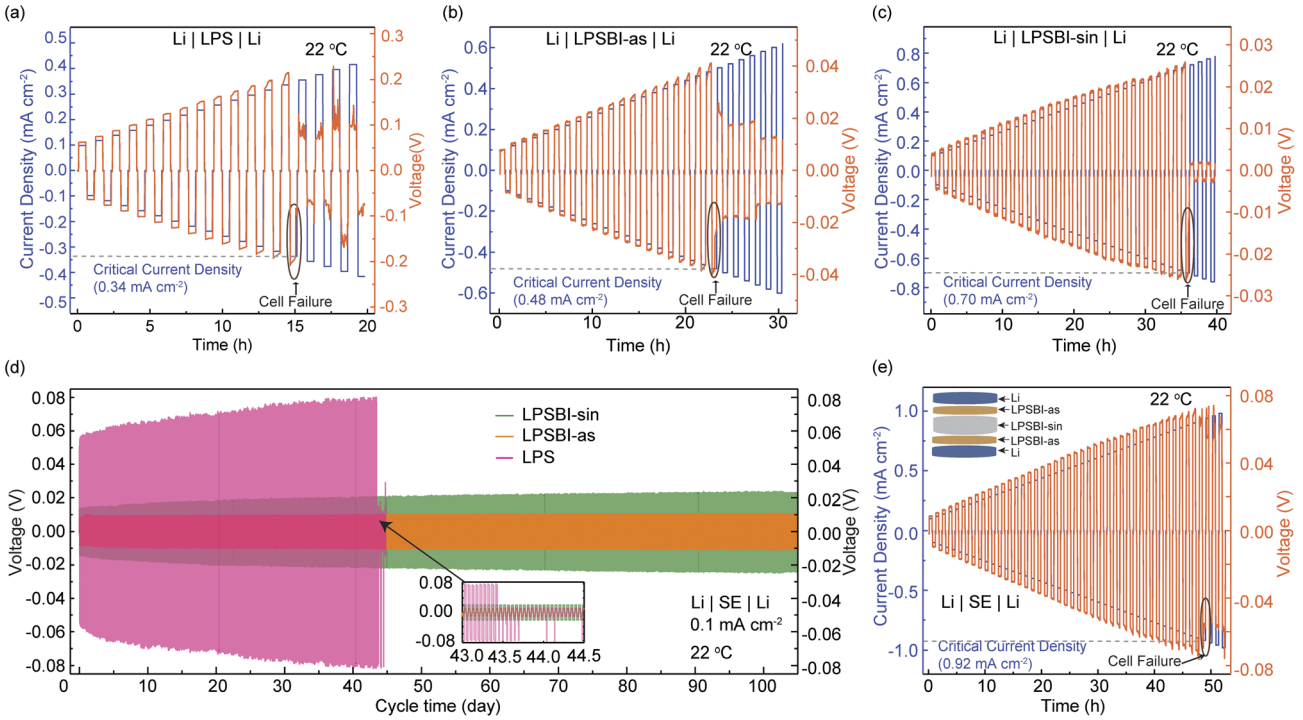

Fig. 2 Electrochemical stability testing of LPSBI against Li metal anodes. Galvanostatic cycling of Li|SE|Li symmetric cells to determine critical current densities using the following SEs: (a) LPS, (b) LPSBI-as, and (c) LPSBI-sin. (d) Long-term stability testing of Li|SE|Li symmetric cells with a current density of 0.1 mA cm^{-2} using LPS, LPSBI-as, and LPSBI-sin as SEs. (e) An improved critical current density of 0.92 mA cm^{-2}, achieved using the sandwiched structure Li|LPSBI-as|LPSBI-sin|LPBSBI-as|Li.

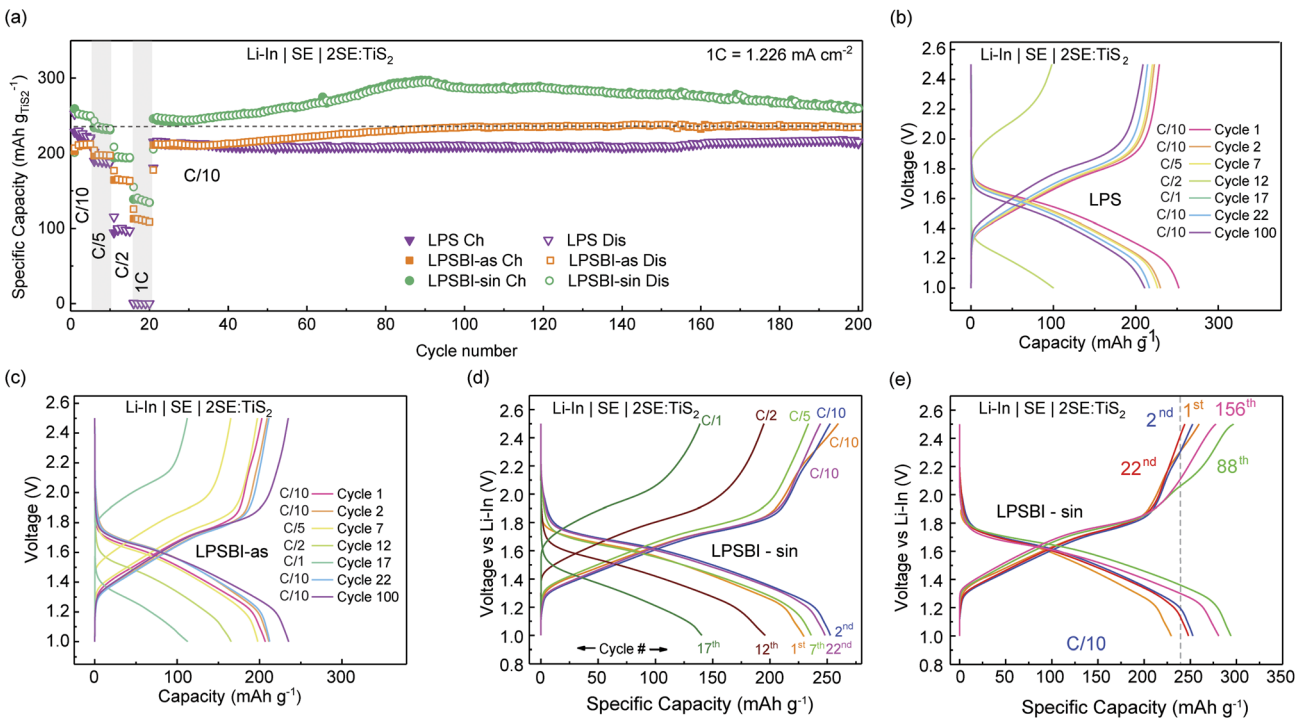

Fig. 3 Half-cell performance of LPS, LPSBI-as, and LPSBI-sin solid electrolytes with TiS_2 as the CAM and Li–In as the anode. (a) Cycle *vs.* capacity at various C-rates (C/10, C/5, C/2, and 1C, corresponding to 0.14 mA cm^{-2}, 0.28 mA cm^{-2}, 0.70 mA cm^{-2}, and 1.40 mA cm^{-2}, respectively) and long-term cycling at C/10 (C = 239 mA g^{-1}). (b–d) Voltage profiles of Li–In|SE|2SE:TiS_2 at different C-rates with LPS, LPSBI-as, and LPSBI-sin as SEs. (e) Voltage profiles of Li–In|SE|2SE:TiS_2 with LPSBI-sin as the SE at C/10 for selected cycles.

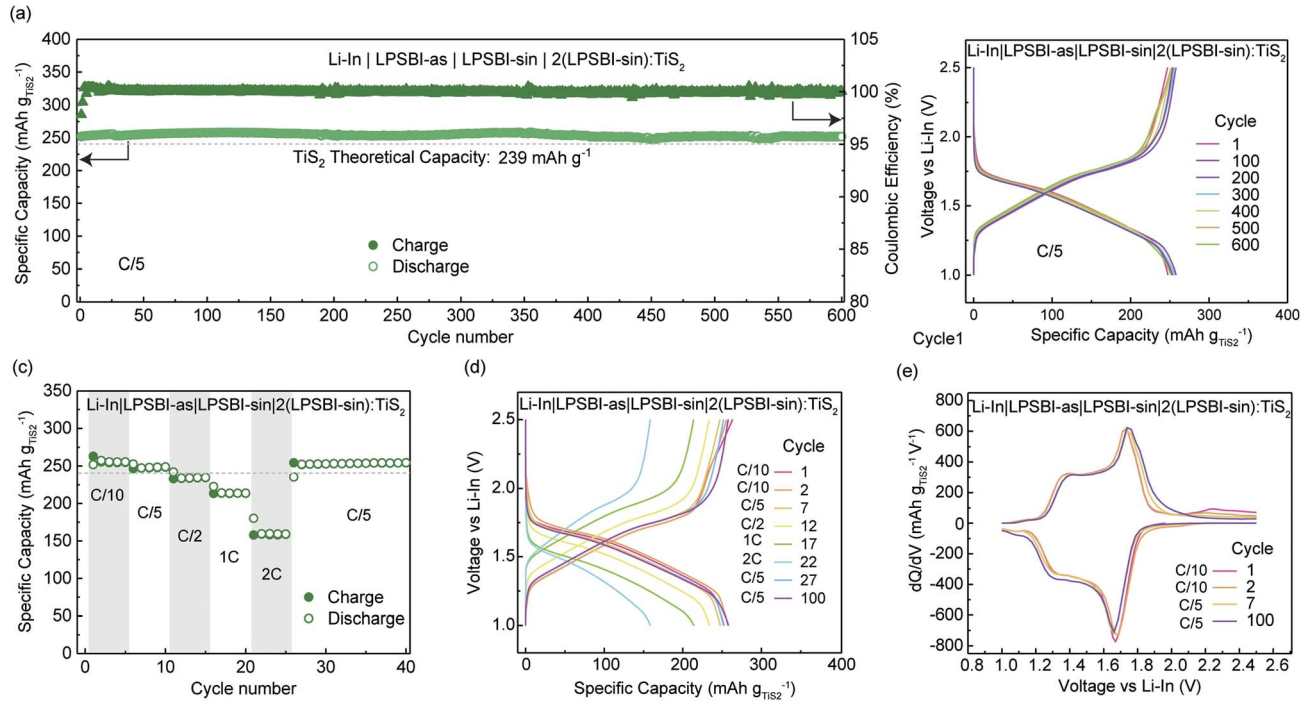

Fig. 4 Electrochemical cycling performance of a Li–In|LPSBI-as|LPSBI-sin|2(LPSBI-sin):TiS_2 cell. (a) Long-term capacity *vs.* cycle number at C/5 for 600 cycles and (b) voltage profiles of selected cycles at C/5. (c) Cycling rate-performance at various C-rates (C/10, C/5, C/2, 1C, 2C) for 40 cycles, (d) voltage profile of selected cycles with different C-rates, and (e) the differential capacity plots of cycles 1, 2, 7, and 100.

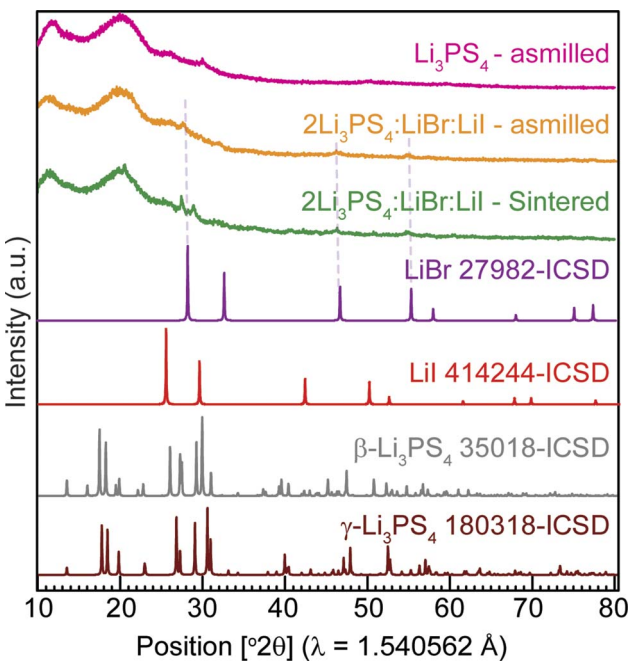

Fig. 5 XRD patterns of LPS, LPSBI-as, and LPSBI-sin and comparison with reference patterns of β-Li_3PS_4, γ-Li_3PS_4, LiBr, and LiI from ICSD.

measurements).[1,2,11] In agreement with the cyclic voltammograms, the quasi-plateau at 1.2 V is assigned to the reduction of the SE to form Li_2S + P, and the plateau at <0.5 V is assigned to lithiation of reduction products such as P to form Li_3P. Both plateaus remain reversible, indicating the effective stability window is larger than the thermodynamic window of the SE.[22] This aligns well with previous experimental reports on stability windows of thiophosphates.[11,23] On the first charge, we see capacity plateaus at 1.8 V, 2.25 V, and 2.4 V *vs.* Li–In. At 1.8 V, this is assigned to $S_x^{2-} \rightarrow S_x$.[11] The plateau at 2.25 V is assigned to the oxidation of I^- (Fig. S5). The capacity plateau at 2.4 V is assigned to the oxidation of PS_4^{3-}, based on previous reports.[11] However, this plateau disappears for later cycles, indicating the formation of a passivation layer after the first cycle.

ASSB half-cell performance. Fig. 3a shows the cycling performance of the SEs in ASSB half-cells using TiS_2 as the CAM. The experimental capacity at C/10 (~250 mAh g^{-1}) is slightly higher than the theoretical capacity of TiS_2 (239 mAh g^{-1}). One reason for this is the additional capacity generated by the redox of the SEs. From the voltage profile plots shown in Fig. 3c and d, the $Ti^{3+/4+}$ plateau at ~1.7 V *vs.* Li–In can be seen, as expected.[23] Fig. 3b–d shows the voltage profiles for the rate performance measurements for LPS-, LPSBI-as-, and LPSBI-sin-containing cells. At 2C (C = 239 mA g^{-1}), a capacity of ~140 mAh g^{-1} for the LPSBI-sin-containing cell is higher than that of LPSBI-as, 112 mAh g^{-1}, and 0 mAh g^{-1} for the LPS-containing cell.

Over long-term cycling at C/10 (see voltage profile of selected cycles in Fig. 3e), the LPSBI-sin cell shows a steady increase in capacity up to ~300 mAh g^{-1} until cycle 88 and then gradually decreases to 236 mAh g^{-1} at cycle 200. A potential reason for this is I^- oxidation, which is not fully reversible (Fig. S8). I^- oxidation is observed at ~2.25 V *vs.* Li–In, which is also seen from the dQ/dV of 3SE:SP-containing cells (Fig. S6). Our dQ/dV

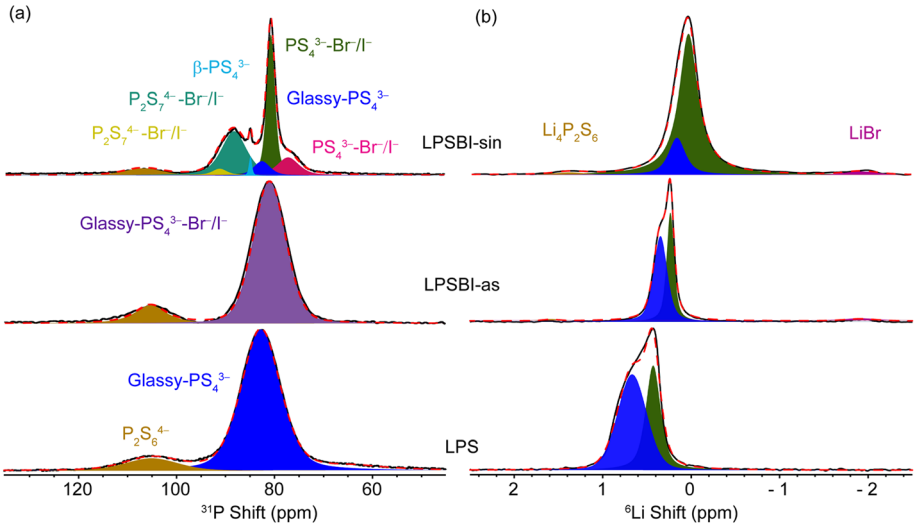

Fig. 6 Local structural characterization of LPS, LPSBI-as, and LPSBI-sin solid electrolytes with (a) ^{31}P and (b) ^{6}Li MAS NMR.

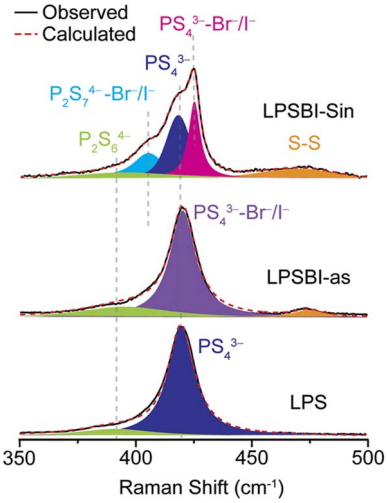

Fig. 7 Raman spectra of LPS, LPSBI-as, and LPSBI-sin.

results on long-term cycling show that the I^- oxidation peak is observed from the 1st cycle to the 88th cycle, but it is lacking for the 156th cycle (Fig. S8). Furthermore, this assignment is confirmed by comparing our galvanostatic cycling results to our previous work using $2(3Li_3PS_4{:}LiBr){:}TiS_2$ catholytes,[1] where we do not observe any capacity at ~2.25 V *vs.* Li–In. Besides the I^- oxidation peak, we observe the onset of another peak for the first cycle at ~2.4 V, which disappears after the first cycle. This peak for the first charge can be assigned to the oxidation of PS_4^{3-}.[11] The LPSBI-as-containing cell shows an increase in capacity for the same reasons; however, the maximum capacity achieved is ~240 mA h g^{-1}, which is significantly lower than that of the LPSBI-sin-containing cell. Conversely, the LPS-containing cell shows no capacity increase upon cycling and shows stable cycling at C/10.

The trends in the stability of the SEs and the effective partial ionic and electronic conductivity of the catholytes closely match the trends in cycling capacity (Fig. S9). All catholytes exhibit a high effective electronic conductivity of ≥95 mS cm^{-1}, with ionic conductivity being the kinetic rate-limiting factor. The

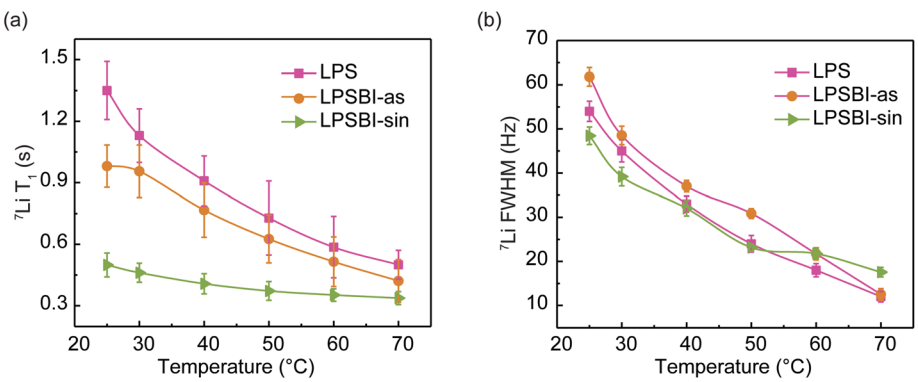

Fig. 8 T_1 NMR-relaxation time analysis to probe ion dynamics (a) variable-temperature ^{7}Li NMR for LPS, LPSBI-as, and LPSBI-sin. (b) Variable-temperature ^{7}Li NMR linewidths (full-width-at-half-maximum, FWHM) for LPS, LPSBI-as, and LPSBI-sin.

LPSBI-sin-containing catholyte shows the highest effective ionic conductivity at 0.026 mS cm^{-1}, compared to LPS (0.001 mS cm^{-1}) and LPSBI-as (0.010 mS cm^{-1}).

Owing to the better stability of LPSBI-as against Li-metal, and the higher CCD achieved with the sandwiched structure Li|LPSBI-as|LPSBI-sin|LPBSBI-as|Li, we assembled ASSB half-cells with two separator layers. A thin layer (25 mg) of LPSBI-as was placed towards the Li–In anode, while LPSBI-sin separator (75 mg) was used towards the cathode. For the catholyte, 2(LPSBI-sin):TiS_2 was used. The performance of the cells showing high rate-capability and stable cycling is presented in Fig. 4. The first discharge capacity of 252 mAh g^{-1} and charge capacity of 253 mAh g^{-1} are achieved at C/5 at room temperature (Fig. 4a and b). As shown in Fig. 4a and b, a very high-capacity retention (>99%) after 600 cycles indicates the high stability and excellent performance of the engineered cell configuration (Li–In|LPSBI-as|LPSBI-sin|2(LPSBI-sin):TiS_2). As shown in Fig. 4c, a high reversible capacity of ~155 mAh g^{-1} is achieved at 2C, followed by excellent retention at C/5. Fig. 4d shows the voltage profiles of selected cycles, and Fig. 4e shows the differential capacity. The capacity from the $Ti^{3+/4+}$ peak at ~1.7 V *vs.* Li–In is prominent, as expected, in addition to another peak at higher voltage (~2.25 V *vs.* Li–In), which can be assigned to I^- oxidation.[23]

Morphology analysis. To understand morphology, compositional homogeneity, and the compatibility of LPSBI-as with Li-metal, SEM images were obtained, and electron-dispersive X-ray spectroscopy (EDS) was performed. Fig. S10 shows the morphology of LPS, LPSBI-as, and LPSBI-sin SEs. As-milled LPS shows a highly homogeneous morphology with very smooth features. In the case of LPSBI-as, two distinct contrasts (dark and bright) are observed, indicating the presence of two morphologies. LPSBI-sin, on the other hand, shows the brighter contrast layer on top of the dark contrast, probably due to the presence of multiple phases. This qualitatively shows the excess iodine phases with bright contrast on top of the less iodine phase morphology. This aligns well with our electrochemical measurements (Fig. 4 and S6), indicating more pronounced iodide oxidation. Grain boundaries and cracks are mostly absent on LPS and LPSBI-as, while more cracks are observed for the LPSBI-sin. It is well established that surface grain boundaries and cracked morphology can lead to surface reactions with Li-metal, increasing the interfacial resistance of the Li-symmetric cell, as observed during long-term symmetric cycling.[24] From EDX of LPSBI-as SE (Fig. S11), the phosphorus, sulfur, and bromine are homogenously distributed on the given morphology of the pellet. However, a more discrete iodine map is shown in the EDX images, which corresponds well with the SEM morphology.

Structural characterization

X-ray diffraction

To determine the long-range structure, we performed powder X-ray diffraction measurements of the three model SEs. The diffraction patterns (Fig. 5) reveal low crystallinity, even for the low-temperature sintered LPSBI-sin. For LPS, small peaks of β-Li_3PS_4 can be identified. A slight trace of LiBr impurity is observed for both LPSBI-as and LPSBI-sin samples, while the LiI impurity is not visible in the powder XRD pattern. This suggests that both LiBr and LiI are incorporated into the LPS framework to get the new glass–ceramic phase, responsible for superionic conduction in LPSBI.

Nuclear magnetic resonance (NMR) spectroscopy

Since the SEs of interest lack any long-range ordering evident from XRD, we examine the short-range structures using solid-state NMR (Fig. 6). Starting with LPS, the main phase, as determined from ^{31}P MAS NMR spectra (Fig. 6a), is located at ~83 ppm and assigned to a glassy PS_4^{3-} unit.[1,2,25] A secondary phase is also observed at ~106 ppm, which is assigned to $P_2S_6^{4-}$.[1,25] The ^{31}P MAS NMR spectra are not significantly different for LPSBI-as compared to those of LPS. With the sintering, LPSBI-sin shows the formation of PS_4^{3-}–Br^-/I^- at ~81 and ~78 ppm, along with the formation of $P_2S_7^{4-}$–Br^-/I^- at around ~91 and ~89 ppm.[26–28] In addition, a trace amount of β-PS_4^{3-} at ~85.5 ppm and glassy-PS_4^{3-} at ~82.5 ppm are observed.[1,2,25]

To understand the local lithium environment of LPS, LPSBI-as, and LPSBI-sin, we performed ^6Li MAS NMR, as shown in Fig. 6b. We observed two distinct resonances corresponding to distinct lithium environments in all three electrolytes, consistent with previous reports.[1,2] The variation in peak position and broadening suggests differences in the lithium local environments and dynamics. The resonance shown in blue (Fig. 6b) is predominant in LPSBI-as and LPS. The intensity of this resonance in LPSBI-sin was reduced significantly, making the resonance in green the dominant Li local environment. It has been reported that the Li site, as indicated by the green resonance (upfield), is more mobile than the blue one (downfield).[1,2] With the incorporation of Br^- and I^- into the LPS framework, further changes in the lithium environment are indicated by shifts in the peaks towards lower ppm values.[1]

Raman spectroscopy

Raman spectroscopy is highly informative for understanding the connectivity of thiophosphate polyhedra (Fig. 7). For LPS, two components were fitted and assigned to glassy-PS_4^{3-} and $P_2S_6^{4-}$. LPSBI-as shows no significant changes, but with slightly more $P_2S_6^{4-}$ and a new peak at ~475 cm^{-1} assigned to S–S stretching.[27] With the sintering, LPSBI-sin shows a new peak around 405 cm^{-1} assigned to $P_2S_7^{4-}$–Br^-/I^-,[26,27] in addition to the peaks from PS_4^{3-} and $P_2S_6^{4-}$.

NMR relaxometry

To probe the lithium-ion dynamics, variable-temperature ^7Li MAS NMR spectra and T_1 relaxation times were acquired. Representative spectra are presented in Fig. S13a, S14a and S15a. Fig. 8 presents the ^7Li spin-lattice relaxation times (T_1) and linewidths as a function of temperature. Fig. S13b, S14b and S15b present the variable-temperature ^{31}P MAS NMR spectra, and Fig. S16 presents the ^{31}P T_1 alongside the line broadening of the SEs. With increasing temperature (Fig. 8b), motional line narrowing becomes evident in the ^7Li MAS NMR spectra of LPS, LPSBI-as, and LPSBI-sin, originating from the

rapid averaging of Li–Li dipolar interactions as Li-ion mobility increases at higher temperatures.[29]

The ^{7}Li T_1 NMR relaxation time for LPS, LPSBI-as, and LPSBI-sin decreases with increasing temperature (Fig. 8a); therefore, a shorter T_1 signifies faster Li^+ motion. Notably, the shorter T_1 for LPSBI-sin at room temperature compared to LPSBI-as and LPS indicates enhanced Li^+ mobility for LPSBI-sin. This observation correlates with the trend in ionic conductivity. The ^{31}P NMR spectrum of LPSBI-sin (Fig. S15b) reveals the presence of multiple distinct phosphorus local environments. As the temperature increases, the line width narrows, suggesting motional averaging. The decrease in T_1 relaxation time of $P_2S_7^{4-}$–Br^-/I^- and PS_4^{3-}–Br^-/I^- relative to PS_4^{3-}, as observed in the ^{31}P VT-NMR experiments, also suggests increased anion motion in LPSBI, which may facilitate fast Li^+ ion conduction.[30]

Conclusion

In this work, Li_3PS_4 with halide incorporation, such as Br^- and I^-, has been shown to significantly enhance ion transport. LPSBI-sin exhibits an ionic conductivity of 4.36 mS cm^{-1} at 25 °C with an activation energy of 0.29 eV. Multinuclear solid-state NMR and Raman spectroscopy show a significant change in the Li^+ local environment upon the incorporation of halides. With Br^- and I^- interspersed within the framework composed of PS_4^{3-} and $P_2S_7^{4-}$, we observe enhanced dynamics of both Li^+ and the anion matrix.

Using a stacked cell with LPSBI-as and LPSBI-sin SEs shows improved cycling performance compared to single-layer SE-containing cells. It demonstrates how cell engineering with different SEs can boost the performance of ASSBs. A maximum critical current density of 0.92 mA cm^{-2} and a specific capacity of around 260 mAh g^{-1} are achieved using TiS_2 as the CAM, showing high-rate performance and over 99% coulombic efficiency and very high-capacity retention (>99%) over 600 cycles. This work shows that the synergistic effects of mixing halides in Li_3PS_4 can significantly enhance Li^+ dynamics and electrochemical performance.

Conflicts of interest

The authors declare no conflict of interest.

Data availability

The data supporting this article have been included as part of the supplementary information (SI). Supplementary information: electrochemical characterization, electrochemical performance tests, structural characterizations, electron microscopy, X-ray diffraction, and variable-temperature NMR. See DOI: https://doi.org/10.1039/d6sc00740f.

Acknowledgements

The authors would like to acknowledge the support from the National Science Foundation under grant no. DMR-2319151. All solid-state NMR experiments were performed at the National High Magnetic Field Laboratory, which is supported by National Science Foundation Cooperative Agreement No. DMR-1644779 and DMR-2128556*. T. P. Poudel and Y.-Y. Hu would like to thank Dr J. S. Raaj Vellore Winfred from the Materials Characterization Lab at the Department of Chemistry and Biochemistry at Florida State University for his help in acquiring the Raman data. The authors would like to thank Dr Xinsong Lin for his assistance with the lab powder X-ray characterization at the Department of Chemistry and Biochemistry at Florida State University.

References

1 T. P. Poudel, M. J. Deck, P. Wang and Y.-Y. Hu, *Adv. Funct. Mater.*, 2024, **34**, 2309656.
2 M. J. Deck, P.-H. Chien, T. P. Poudel, Y. Jin, H. Liu and Y.-Y. Hu, *Adv. Energy Mater.*, 2024, **14**, 2302785.
3 P. Wang, S. Patel, J. E. Roberts, B. E. Francisco and Y.-Y. Hu, *ACS Mater. Lett.*, 2024, **6**, 2059–2064.
4 H. Stöffler, T. Zinkevich, M. Yavuz, A. Senyshyn, J. Kulisch, P. Hartmann, T. Adermann, S. Randau, F. H. Richter, J. Janek, S. Indris and H. Ehrenberg, *J. Phys. Chem. C*, 2018, **122**, 15954–15965.
5 Z. Liu, W. Fu, E. A. Payzant, X. Yu, Z. Wu, N. J. Dudney, J. Kiggans, K. Hong, A. J. Rondinone and C. Liang, *J. Am. Chem. Soc.*, 2013, **135**, 975–978.
6 Y. Zeng, B. Ouyang, J. Liu, Y.-W. Byeon, Z. Cai, L. J. Miara, Y. Wang and G. Ceder, *Science*, 2022, **378**, 1320–1324.
7 P. Minnmann, L. Quillman, S. Burkhardt, F. H. Richter and J. Janek, *J. Electrochem. Soc.*, 2021, **168**, 040537.
8 M. J. Deck and Y.-Y. Hu, *J. Mater. Res.*, 2023, **38**, 2631–2644.
9 S. V. Patel, S. Banerjee, H. Liu, P. Wang, P.-H. Chien, X. Feng, J. Liu, S. P. Ong and Y.-Y. Hu, *Chem. Mater.*, 2021, **33**, 1435–1443.
10 S. Ohno, C. Rosenbach, G. F. Dewald, J. Janek and W. G. Zeier, *Adv. Funct. Mater.*, 2021, **31**, 2010620.
11 G. F. Dewald, S. Ohno, M. A. Kraft, R. Koerver, P. Till, N. M. Vargas-Barbosa, J. Janek and W. G. Zeier, *Chem. Mater.*, 2019, **31**, 8328–8337.
12 T. P. Poudel, E. Truong, I. P. Oyekunle, M. J. Deck, B. Ogbolu, Y. Chen, P. K. Ojha, T. N. D. D. Gamaralalage, S. V. Patel, Y. Jin, D. Hou, C. Huang, T. Li, Y. Liu, H. Xiong and Y.-Y. Hu, *ACS Energy Lett.*, 2025, **10**, 40–47.
13 T. P. Poudel, I. P. Oyekunle, M. J. Deck, Y. Chen, D. Hou, P. K. Ojha, B. O. Ogbolu, C. Huang, H. Xiong and Y.-Y. Hu, *Chem. Sci.*, 2025, **16**, 2391–2401.
14 I. P. Oyekunle, E. Truong, T. P. Poudel, Y. Chen, Y. Jin, I. A. Ojelade, M. J. Deck, B. Ogbolu, M. M. Islam, P. K. Ojha, J. S. R. V. Winfred, D. Hou, H. Xiong, C. Huang and Y.-Y. Hu, *Chem. Sci.*, 2025, **16**, 10372–10385.
15 R. B. Nuernberg, *Ionics*, 2020, **26**, 2405–2412.
16 S. V. Patel, E. Truong, H. Liu, Y. Jin, B. L. Chen, Y. Wang, L. Miara, R. Kim and Y.-Y. Hu, *Energy Storage Mater.*, 2022, **51**, 88–96.
17 I. Hanghofer, M. Brinek, S. L. Eisbacher, B. Bitschnau, M. Volck, V. Hennige, I. Hanzu, D. Rettenwander and H. M. R. Wilkening, *Phys. Chem. Chem. Phys.*, 2019, **21**, 8489–8507.

18 B.-Y. Chang, *J. Electrochem. Sci. Technol.*, 2020, **11**, 318–321.
19 R. Schlem, A. Banik, S. Ohno, E. Suard and W. G. Zeier, *Chem. Mater.*, 2021, **33**, 327–337.
20 Y. Lu, C. Zhao, H. Yuan, X. Cheng, J. Huang and Q. Zhang, *Adv. Funct. Mater.*, 2021, **31**, 2009925.
21 F. Han, Y. Zhu, X. He, Y. Mo and C. Wang, *Adv. Energy Mater.*, 2016, **6**, 1501590.
22 S. Banerjee, M. L. H. Chandrappa and S. P. Ong, *ACS Appl. Energy Mater.*, 2022, **5**, 35–41.
23 B. T. Leube, C. Robert, D. Foix, B. Porcheron, R. Dedryvère, G. Rousse, E. Salager, P.-E. Cabelguen, A. M. Abakumov, H. Vezin, M.-L. Doublet and J.-M. Tarascon, *Nat. Commun.*, 2021, **12**, 5485.
24 A. Shastri, N. Rons, Q.-P. Ding, S. J. Kmiec, M. Olson, Y. Furukawa and S. W. Martin, *Solid State Ionics*, 2023, **402**, 116363.
25 X. Chi, Y. Zhang, F. Hao, S. Kmiec, H. Dong, R. Xu, K. Zhao, Q. Ai, T. Terlier, L. Wang, L. Zhao, L. Guo, J. Lou, H. L. Xin, S. W. Martin and Y. Yao, *Nat. Commun.*, 2022, **13**, 2854.
26 R. Rajagopal, Y. Subramanian and K.-S. Ryu, *ACS Sustainable Chem. Eng.*, 2023, **11**, 2692–2703.
27 A. Kato, M. Yamamoto, F. Utsuno, H. Higuchi and M. Takahashi, *Commun. Mater.*, 2021, **2**, 1–8.
28 H. Tsukasaki, S. Mori, S. Shiotani and H. Yamamura, *Solid State Ionics*, 2018, **317**, 122–126.
29 B. B. Duff, S. J. Elliott, J. Gamon, L. M. Daniels, M. J. Rosseinsky and F. Blanc, *Chem. Mater.*, 2023, **35**, 27–40.
30 P. Wang, H. Liu, S. Patel, J. E. Roberts, Y. Chen, B. Ogbolu, B. E. Francisco and Y.-Y. Hu, *Adv. Energy Mater.*, 2024, **14**, 2401549.